Accepted Manuscript

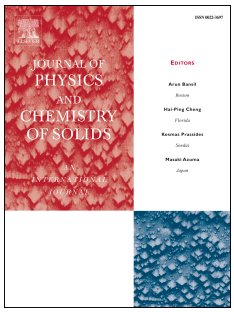

Atomistic modeling of grain boundary behavior under shear conditions in magnesium and magnesium-based binary alloys

M.K. Nahhas, S. Groh

PII: S0022-3697(17)30928-9

DOI: 10.1016/j.jpcs.2017.10.017

Reference: PCS 8247

To appear in: *Journal of Physics and Chemistry of Solids*

Received Date: 26 May 2017

Revised Date: 2 October 2017

Accepted Date: 12 October 2017

Please cite this article as: M.K. Nahhas, S. Groh, Atomistic modeling of grain boundary behavior under shear conditions in magnesium and magnesium-based binary alloys, *Journal of Physics and Chemistry of Solids* (2017), doi: 10.1016/j.jpcs.2017.10.017.

Atomistic modeling of grain boundary behavior under shear conditions in magnesium and magnesium-based binary alloys

M.K. Nahhas and S. Groh*

Department of biomedical engineering, University of Basel, 4123 Allschwil, Switzerland

Abstract In this study, the structure, the energetic, and the strength of a $\{10\bar{1}1\}\langle 11\bar{2}0\rangle$ symmetric tilt grain boundary in magnesium and magnesium binary alloys were analyzed in the framework of (semi-)empirical potentials. Following a systematic investigation of the transferability and accuracy of the interatomic potentials, atomistic calculations of the grain boundary energy, the grain boundary sliding energy, and the grain boundary strength were performed in pure magnesium and in binary MgX alloys (X = Al, Ca, Gd, Li, Sn, Y, Ag, Nd, and Pb). The data gained in this study were analyzed to identify the most critical material parameters controlling the strength of the grain boundary, and their consequence on atomic shuffling motions occurring at the grain boundary. From the methodology perspective, the role of in-plane and out-of plane relaxation on the grain boundary sliding energy curves was investigated. In pure magnesium, the results showed that in-plane relaxation is critical in activating $b_2^{\{10\bar{1}1\}}$ twinning dislocation resulting in grain boundary migration. In the alloy systems, however, grain boundary migration was disabled as a consequence of the pinning of the grain boundary by segregated elements. Finally, while the grain boundary energy, the shape of the grain boundary sliding energy curves, and the grain boundary sliding energy are critical parameters controlling the grain boundary strength in pure magnesium, only the grain boundary energy and the segregation energy of the alloying elements at the grain boundary were identified as critical material parameters in the alloys system.

Keywords: magnesium binary alloys; grain boundaries; molecular statics; segregation energies; defects; anelasticity; mechanical properties; metals

1. Introduction

As a consequence of the high plastic anisotropy at low and room temperature between basal and non-basal slip in magnesium, additional deformation modes to dislocation-based plasticity have to be taken into consideration when modeling the inelastic behavior of magnesium. While several deformation modes could be listed, this study focuses on (i) the properties of symmetrical tilt grain boundary, and (ii) on the mechanism of grain boundary sliding. Since grain boundary sliding is a major deformation mode in fine-grained magnesium, the control of such deformation mode in magnesium and its alloys would offer a solution to improve the formability of magnesium and its alloys.

* Corresponding author: fax:+41-61-2075409
E-mail address: Sebastien.Groh@unibas.ch (S. Groh)

Experimentally, Somekawa and Mukai [1] investigated, by performing nanoindentation creep test, the role of the grain boundary structure on the deformation behavior of magnesium and magnesium binary alloys. These authors revealed a decrease of the grain boundary energy, and thus, suppressing grain boundary sliding when considering magnesium alloyed with Al solute element. Furthermore, Somekawa et al. [2] analyzed experimentally the effect of alloying elements in the solid solution approximation on grain boundary sliding using pure magnesium and six kinds of alloying elements (Ag, Al, Li, Pb, Y, and Zn). While the amount of grain boundary sliding was reduced/suppressed with the addition of alloying elements, the data presented by the authors suggest that Y and Ag are more effective alloying elements than Zn, Al, and Li in suppressing grain boundary sliding.

A few research groups proposed strengthening design maps based on first-principles data to quantify the effect of alloying elements on specific symmetric tilt grain boundaries (STGB). Zhang et al. [3] performed first-principles calculations to reveal the effect of a large group of solute elements on the segregation energy at a $\{01\bar{1}2\}\langle 10\bar{1}1\rangle$ tension twin. Segregation of bigger and smaller solute elements at the twin boundary is possible as a consequence of the presence of expanded and contracted lattice sites at the grain boundary, respectively. The substitution of bigger/smaller solute elements at the expanded/contracted lattice sites compensates the lattice distortion leading to a decrease of the total energy of the binary system compared to the one obtained in the pure system. By correlating the segregation energy with the solute diffusion activation enthalpy, the authors proposed a strengthening map of the $\{01\bar{1}2\}\langle 10\bar{1}1\rangle$ tensile twin that include a wide variety of solute elements. From their data it appears that solute elements having the highest probability of segregation and the highest probability of diffusion are leading to the larger strengthening of the twin boundary. Within the same idea, Xi et al. [4] analyzed the strengthening/embrittlement tendency of the $\{10\bar{1}1\}\langle 11\bar{2}0\rangle$ twin boundary using first-principles calculations by evaluating the resistance of the interface to decohesion. These authors characterized the resistance of the interface to decohesion as the segregation energy difference between the interface and the free surface. Similarly to Zhang et al. [3], Xi et al. [4] revealed the presence of contracted and expanded lattice sites at the twin boundary, and reported the magnitude of the segregation energy for a large group of solute elements in both the contraction and expansion lattice sites. These authors proposed a design map by correlating the segregation energy at the twin boundary with the resistance of the interface to decohesion. Such a design map suggests that alloying elements from the d-block as well as rare earth alloying elements are promising candidates to strengthen the $\{10\bar{1}1\}\langle 11\bar{2}0\rangle$ twin boundary. Finally, Huber et al. [5] employed first-principles calculations to study the interaction between a large group of alloying elements with a $\Sigma 7$ grain boundary (GB) in magnesium. Since their numerical data revealed a correlation between the binding energy and (i) the size of the solute element at the GB, and (ii) the local grain boundary volumes, these authors proposed an elastic model to capture the variation of the binding energy as a function of the two aforementioned parameters.

Grain-boundary mediated plasticity, with mechanisms such as grain boundary sliding, grain boundary migration, and grain boundary rotation, is an additional deformation mode to dislocation-mediated plasticity. Recently, Bhatia et al. [6] quantified the grain boundary sliding energy barrier from the grain boundary sliding energy (GBSE) curve, while Barrett et al. [7] proposed the so-called generalized interfacial fault energy (GIFE) curve to quantify the energy barrier for grain boundary migration normal to the interface plane. Both the GBSE and the GIFE curves were thought to quantify the contribution of grain boundary sliding and grain boundary migration to the overall mechanical behavior. Using the GBSE metric, Bhatia et al. [6] concluded that a random distribution of Y solute elements in the vicinity of the $\{10\bar{1}1\}\langle 11\bar{2}0\rangle$ STGB has a softening effect on the grain boundary. Therefore, these authors excluded solute solution strengthening of the grain boundary as a possible mechanism to explain the experimentally observed strengthening enhancement due to the presence of Y in polycrystalline magnesium-based alloys.

Using large-scale molecular dynamics calculations in the framework of (semi-)empirical potentials, Reddy and Groh [8] revealed the effect of a low concentration of segregated Ca alloying elements on the yield surfaces of nanopolycrystalline MgCa alloys. These authors concluded that segregation of Ca alloying elements enhances intergranular fracture. Using the metric proposed by Bhatia et al. [6], the conclusion of Reddy and Groh suggests that segregated Ca alloying elements increases the grain boundary sliding energy barrier. Within the same idea, Karewar et al. [9] investigated numerically the effect of a random distribution of Li alloying elements on the ductility of magnesium-based alloys using empirical potentials. These authors revealed a decrease of the plastic anisotropy by enhancing the activity of the non-basal slip system and tension twinning $\{10\bar{1}2\}\langle 10\bar{1}1\rangle$.

The objectives of this study are twofold. Firstly, the influence of intrinsic material parameters on the strength of the $\{10\bar{1}1\}\langle 11\bar{2}0\rangle$ STGB in pure magnesium bicrystal are identified, and associated with the mechanisms occurring at the grain boundary under an applied shear stress. Secondly, once the transferability and the accuracy of the (semi-)empirical potentials describing the MgX binary systems (X = Al, Ca, Gd, Li, Sn, Y, Ag, Nd, and Pb) for modeling grain boundary/solute element interactions are validated with regards to either first-principles data or elastic theory, the effect of alloying elements (Al, Ca, Gd, Li, Sn, Y, Ag, Nd, and Pb) on the intrinsic material parameters available to characterize the $\{10\bar{1}1\}\langle 11\bar{2}0\rangle$ STGB are quantified. Finally, the changes in mechanisms occurring at the grain boundary in MgX binary alloys are discussed in comparison to the ones obtained in pure magnesium bicrystal.

In this manuscript, the methodology used to calculate the energetic of STBG in pure and in binary magnesium-based alloys is presented in Section 2 in addition to a succinct review of the (semi-)empirical potentials available for the MgX binary systems. In Section 3, the physical and mechanical properties of the $\{10\bar{1}1\}\langle 11\bar{2}0\rangle$ STGB calculated with different magnesium models are presented. In addition, the change in grain boundary energy, grain boundary sliding energy barrier, and their relation to the critical shear stress due to presence of alloying

elements are presented in Section 3 as well. The numerical data are discussed in Section 4. Concluding remarks are given in Section 5.

2. Method

2.1 Interatomic potential available in the literature for MgX binary alloys

If one wants to identify the structure/property relations in crystalline materials using classical molecular dynamics simulations, the accuracy of the generated data strongly depends on the transferability of the (semi-)empirical potentials [10]. As reported by Zu and Groh [11], a large number of (semi-)empirical potentials for modeling MgX binary systems (X = Al, Ca, Gd, Li, Sn, Y, Ag, Nd, and Pb) were developed in the framework of the (modified) embedded-atom method, (M)EAM. As reported in Table 1, these potentials for the binary systems were derived from six specific magnesium models [12-17]. While these potentials were used extensively to reveal structure/property relation in pure magnesium, Groh and Nahhas [18] reviewed their accuracy and transferability in view of modeling dislocations and fracture related issues.

As listed in Table 1, the MgX (X=Al, Li, Y, Sn, Ca, Pb, Nd) potentials proposed by Lee and coworkers [14,19-21], and the MgCa proposed by Groh [22] were derived from the pure magnesium potential proposed by Kim et al. [14]. Using the magnesium potential recently proposed by Wu et al. [17], Groh developed models for MgAg and MgY [23, 24]. The MgLi potential of Karewar et al. [25], and MgAl potential of Mendelev et al. [26] were developed using the magnesium EAM potential proposed by Sun et al. [13]. All the other MgX potentials listed in Table 1 have unique magnesium potential. Using the different MgX potentials listed in Table 1, the atomic volume difference defined as, $\Delta V_{bulk}^{X} = V_{bulk}^{MgX} - V_{bulk}^{Mg}$, where V_{bulk}^{MgX} and V_{bulk}^{Mg} are the volumes obtained under zero pressure of two periodic systems made of (*(N-1)* magnesium atoms and one substitutional atom) and N magnesium atoms, respectively, were calculated. Moreover, the misfit strains defined as $(a^X\text{-}a^{Mg})/a^{Mg}$ and $(c^X\text{-}c^{Mg})/c^{Mg}$, where ($a^{Mg}$, c^{Mg}) and (a^X, c^X) are the lattice parameters of magnesium and of the alloying element *X* crystalized in the hcp crystal structure were evaluated. It should be noted, however, that a comparison between the atomic volume difference and the misfit strains is not straightforward, since the atomic volume difference represents the relaxed volume of a substitutional point defect *X*. Since the Jelinek et al. [16] potential predicted the sign of the formation energy of substitutional Al point defect in magnesium in disagreement with first-principles data while it predicts the sign of the atomic volume difference in agreement with first-principles data, the misfit strains were not predicted with this potential. From the simple analysis of the atomic volume difference listed in Table 1, the MgLi potential of Karewar et al. [25] as well as MgSn potential of Kim et al. [20] do not capture the physics involves in the substitution of alloying elements in magnesium. As a consequence, these two potentials were not considered for our study.

Although alloying elements reported in Table 1 were considered as potential candidates for the biomedical or the transportation industries, the possibility of testing a large number of alloying elements increases the statistical analysis

when revealing the structure/property relations, and validating/disproving/enriching continuum models. Since the potentials reported in Table 1 were developed with the aim of modeling the mechanical properties of magnesium-based alloys, some of these potentials were already used to model the interaction between solute elements and dislocations [27-31], between solute elements and grain boundaries [32, 33], and to perform 'in silico' testing of nanopolycrystalline MgX alloys [6, 8, 9, 34]. However, the transferability to model the interaction between solute elements and grain boundaries of the potentials listed in Table 1 was not validated yet. Therefore, it is critical to assess the accuracy of the (semi-)empirical potentials for the binary system MgX listed in Table 1 in view of identifying the ones that accurately capture the interaction between alloying elements and grain boundaries. In this work, molecular statics calculations were performed using the (M)EAM implementations of the LAMMPS package [35], and atomic configurations were visualized using the OVITO package [36].

Table 1. Atomic volume difference, $\Delta V_{bulk}^{X} = V_{bulk}^{MgX} - V_{bulk}^{Mg}$, and misfit strain, $(a^X\text{-}a^{Mg})/a^{Mg}$ and $(c^X\text{-}c^{Mg})/c^{Mg}$ obtained with the different potentials available in the literature to model MgX binary systems. In italic are the potentials predicting the atomic volume difference opposite with first-principles data [5, 11].

X	Mg Model	MgX Model	ΔV_{bulk}^{X} (Å^3)	$(a^X\text{-}a^{Mg})/a^{Mg}$	$(c^X\text{-}c^{Mg})/c^{Mg}$
Ag	Wu[a]	Groh[n]	-11.67	-0.099	-0.092
Al	Sun[b]	Mendelev[g]	-7.8	-0.106	-0.084
	Liu[c]	Liu[c]	-12.09	-0.118	-0.059
	Kim[d]	Kim[d]	-6.99	-0.117	-0.077
	Jelinek[e]	Jelinek[e]	-4.54		
Li	*Sun[b]*	*Karewar[h]*	*3.22*	*-0.018*	*-0.015*
	Kim[d]	Kim[i]	-3.05	-0.031	-0.022
Sn	Kim[d]	*Kim[j]*	*6.41*	*0.072*	*0.08*
Pb	Kim[d]	Kim[k]	-4.41	0.089	0.102
Ca	Kim[d]	Kim[j]	13.35	0.227	0.246
	Kim[d]	Groh[l]	13.96	0.227	0.246
Y	Pei[f]	Pei[f]	11.01	0.141	0.111
	Kim[d]	Kim[j]	5.58	0.137	0.106
	Wu[a]	Groh[m]	8.23	0.138	0.121
Nd	Lee[d]	Kim[k]	13.47	0.094	0.091

[a] [17]; [b] [13]; [c] [12]; [d] [14]; [e] [16]; [f] [15]; [g] [26]; [h] [25]; [i] [19]; [j] [20]; [k] [21]; [l] [22]; [m] [24]. [n] [23].

2.2 Energetic of grain boundary in pure magnesium

The grain boundary energy is calculated as follows:

$$E_{(mn\overline{m+n}k)}^{GB} = \frac{E_1 - N.E_c^{Mg}}{A_{GB}} - 2E_{(mn\overline{m+n}k)}^{S} \quad (1)$$

where E_c^{Mg}, A_{GB}, and $E_{(mn\overline{m+n}k)}^{S}$ are the cohesive energy, the area of the grain boundary, and the energy of the $(mn\overline{m+n}k)$ surface. The total energy, E_1, is

obtained directly by energy minimization of a system containing *N* atoms, a grain boundary and two surfaces. The calculations were performed by setting the two surfaces parallel to the grain boundary plane as free, and applying periodic boundary conditions along the other two directions.

The grain boundary energies obtained with the different magnesium potentials are summarized in Table 2.

2.3 Energetic of grain boundary in binary magnesium alloys

The segregation energy for substitutional element X at the atomic site *i* with location $\boldsymbol{R}_i$ near the grain boundary is defined as:

$$E_{seg}(\boldsymbol{R}_i) = \left(E_{GB}^{MgX}(\boldsymbol{R}_i) - E_{Bulk}^{MgX}\right) - \left(E_{GB}^{Mg} - E_{Bulk}^{Mg}\right) \quad (2)$$

where $E_{GB}^{MgX}(\boldsymbol{R}_i)$ is the total energy of a system containing a STGB and a substitutional point defect *X* at the location $\boldsymbol{R_i}$ near the grain boundary, and E_{GB}^{Mg} is the total energy of the same bicrystal without substitutional point defect. E_{Bulk}^{MgX} and E_{Bulk}^{Mg} are the total energies of a periodic system with and without substitutional point defect.

From the knowledge of the segregation energy profile along the direction normal to the grain boundary, the change in grain boundary energy, $\Delta E_{GB}^{\approx,l}$, due to a concentration, *c,* of alloying elements can be approximated as:

$$\Delta E_{GB}^{\approx,l}(c) = \sum_{k=1}^{N_p}\sum_{i=1}^{N_k}\frac{c_k}{a_{k,i}}\delta_i E_{seg}(\boldsymbol{R}_i) \text{ with } c_k = 1/N_k \text{ and } a_{k,i} = A_{GB}/N_k \quad (3)$$

where N_p is the number of planes parallel to the grain boundary, N_k is the number of atomic sites on the plane *k*. δ_i equals one when substitution occurs at the atomic site *i* of plane k, while δ_i equals zero when substitution does not occur. $a_{k,i}$ represents the area of the atomic site *i* parallel to the grain boundary. For simplicity reason, $a_{k,i}$ is taken as the area of the grain boundary, $A_{GB,}$ divided by the number of atoms in the plane *k*, N_k. It should be noted that since we are considering a linear summation of the segregation energies at the atomic sites where substitution occurs to evaluate the change in grain boundary energy, the change of grain boundary energy due to the presence of alloying elements given by Eq. (3) does not include the interactions among alloying elements themselves.

If one assumes a constant segregation energy defined as the maximum of the segregation energy obtained along the direction normal to the grain boundary, Eq. (3) reduces to:

$$\Delta E_{GB}^{\approx,u}(c) = \frac{E_{seg}^{max}}{A_{GB}}\sum_{k=1}^{N_p}\sum_{i=1}^{N_k}\delta_i = \frac{E_{seg}^{max}}{A_{GB}}N \text{ with } E_{seg}^{max} = max\left[E_{seg}(\boldsymbol{R}_i)\right] \quad (4)$$

where *N* is the number of atomic sites where substitution of magnesium by alloying elements occurred. While Eq. (3) and (4) define the lower and upper bounds of the change of grain boundary energy due to the presence of alloying

elements, these two equations lead to the same prediction for low concentration of alloying elements in/near the grain boundary, while the divergence occurs for large concentration of alloying elements.

In addition, the change in grain boundary energy due to the presence of alloying elements in or near the grain boundary can be derived from direct molecular statics calculations. Therefore, the calculated grain boundary energy change due to the presence of alloying element is obtained as the difference of energy between the one obtained for the grain boundary configuration containing a concentration c of alloying elements substituted in/near the grain boundary and the reference energy obtained in the pure magnesium bicrystal. The calculated grain boundary energy change, $\Delta E_{GB}^{MS}(c)$, is then obtained as:

$$\Delta E_{GB}^{MS}(c) = \frac{\left(E_{GB}^{MgX}(c) - E_{Bulk}^{MgX}(c)\right) - \left(E_{GB}^{Mg} - E_{Bulk}^{Mg}\right)}{A_{GB}} \quad (5)$$

While interatomic interactions among alloying elements is not included in Eq. (3) and (4), these interactions are explicitly taken into consideration in Equation 5 when the distance between two solute elements is smaller than the potential cutoff or the distance between second nearest neighbors.

3. Results

3.1 Grain boundary properties in pure magnesium

Wang and Beyerlein [37] analyzed the dislocation structures of $\langle 11\bar{2}0\rangle$ STGB in magnesium using the potential of Liu et al. [12]. These authors found, in agreement with first-principles data, four STGB with minimum energies. From their data, the $\{10\bar{1}1\}$ STGB has the lowest energy, while the $\{\bar{2}021\}$ STGB has the highest energy out of the four. As a validation test of the grain boundary setting and the relaxation procedure used in this study, the $\{10\bar{1}1\}$, $\{10\bar{1}2\}$, and $\{10\bar{1}3\}$ grain boundary energies were calculated using the six available magnesium empirical models. As reported in Table 2, a perfect match between the $\{10\bar{1}1\}$, $\{10\bar{1}2\}$, and $\{10\bar{1}3\}$ grain boundary energies calculated in this work and the ones reported by Wang and Beyerlein [37] was found when considering the Liu et al. potential. Furthermore, apart from the predictions obtained with the Pei et al. potential [15], for which the $\{10\bar{1}1\}$ grain boundary is not the one with the lowest minimum energy (see Table 2), all the other magnesium potentials lead to a similar trend than the one reported by Wang and Beyerlein, i.e. $E_{GB}^{\{10\bar{1}1\}} < E_{GB}^{\{10\bar{1}3\}} < E_{GB}^{\{10\bar{1}2\}}$.

The $\{10\bar{1}1\}\langle 11\bar{2}0\rangle$ STGB relaxed structure obtained in the framework of the (semi-)empirical potentials is given in Figure 1. Independently of the magnesium model, as presented in Figure 1, the thickness of the $\{10\bar{1}1\}\langle 11\bar{2}0\rangle$ STGB is about 10Å. By analyzing the atomic volume obtained by Voronoi post-processing, four extension sites (e1, e2, e3, and e4) and two compression sites (c1 and c2) compose the grain boundary. As reported in Figure 1B, the atomic sites with maximum compression and extension are located at the same level, i.e. in the plane of the GB. Quantitatively, over the thickness of 10Å, the grain boundary is

composed to 80% of atomic sites c2, e2, e3, e4 (20% each), and 20% of atomic sites c1, and e1 (10% each). The knowledge of the atomic site distribution over the grain boundary thickness is critical in quantifying segregation of solute elements at the grain boundary.

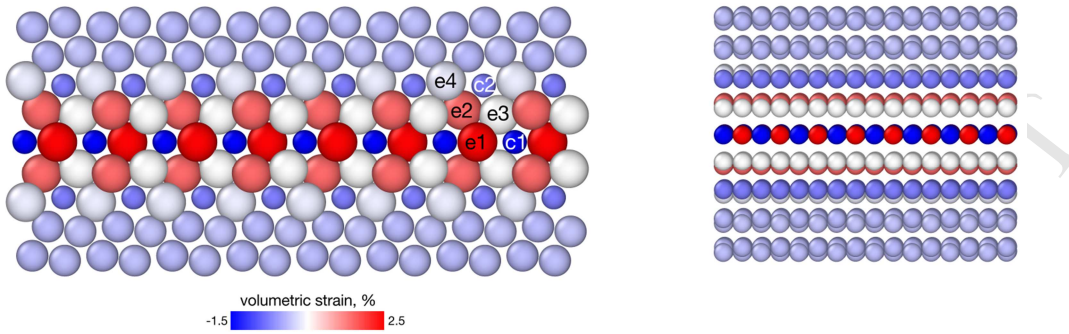

(A) (B)

Figure 1. Atomic structure of the $\{10\bar{1}1\}$ STGB modeled in the modified embedded-atom method framework. (A) Projection of the STGB in the x-z plane. (c1, c2) and (e1, e2, e3, e4) are the contraction and extension atomic sites, respectively. (B) Projection of the STGB in the x-y plane. Atoms are colored based on the volumetric strain. Atoms with small and large radii have negative and positive volumetric strain, respectively.

Table 2. Summary of the grain boundary energies (in mJ/m^2), and relaxed and unrelaxed grain boundary energy barriers (in mJ/m^2) predicted by the magnesium interatomic potentials from the literature. The unrelaxed grain boundary sliding energy barrier, $\gamma_{us}^{(u)}$, was obtained with out-of-plane relaxation only, while the relaxed grain boundary sliding energy barriers, $\gamma_{s}^{(r)}$ and $\gamma_{us}^{(r)}$ were obtained with both in-plane and out-of-plane relaxation.

Mg Model	GB energy (mJ/m^2)			GB interfacial energy (mJ/m^2)		
				Unrelaxed	Relaxed	
	$\{10\bar{1}1\}$	$\{10\bar{1}2\}$	$\{10\bar{1}3\}$	$\gamma_{us}^{(u)}$	$\gamma_{s}^{(r)}$	$\gamma_{us}^{(r)}$
Sun[a]	128	144	143	221	108	120
Liu[b]	79	124	111	178	131	139
Pei[c]	113	160	86	135	73	96
Kim[d]	89	157	109	254	174	180
Wu[e]	90	152	102	257	181	185

[a] [13]; [b] [12]; [c] [15]; [d] [14]; [e] [17].

To calculate the GBSE curve, Bhatia et al. [6] constrained the atoms in the in-plane direction (direction parallel to the grain boundary plane and perpendicular to the displacement direction) by not allowing atomic relaxation in that direction, in addition of constraining the out-of-plane relaxation (direction normal to the grain boundary plane). However, it was reported in several studies that out-of-plane, and in-plane relaxation may significantly influence the generalized stacking fault energy curve [38, 39].

Since it is well known that the magnitude of the generalized stacking fault energy is decreased by out-of-plane relaxation compared to the one obtained without

out-of-plane relaxation, the influence of the out-of-plane relaxation on the magnitude of the unstable grain boundary energy barrier was investigated. Independently of the potential, the shape of the GBSE curve is single humped, and the magnitude of the unstable fault energy obtained for a displacement of *0.5a* along the $\langle 11\bar{2}0 \rangle$ is significantly decreased when considering out-of-plane relaxation. Thus, the Pei et al. potential [15] predicted a decrease of the unstable fault energy from from 325 mJ/m^2 to 135 mJ/m^2 when considering out-of-plane relaxation. Similarly, the Sun et al. potential [13] predicted a decrease from 346 mJ/m^2 to 221 mJ/m^2. A decrease of the unstable fault energy from 276 mJ/m^2 to 178 mJ/m^2, and from 436 mJ/m^2 to 257 mJ/m^2 were obtained with the Liu et al. [12] and Wu et al. [17] potentials, respectively. Finally, the Kim et al. potential [14] predicted a decrease from 412 mJ/m^2 to 254 mJ/m^2 of the unstable fault energy when considering out-of-plane relaxation.

The consequences of in-plane relaxation on the GBSE curves are more severe than out-of-plane relaxation. When considering the generalized stacking fault energy curve, the in-plane relaxation can affect (i) the magnitude of the stable/unstable stacking fault energy [40], (ii) the location of the unstable/stable stacking fault energies [39], and (iii) the overall shape of the generalized stacking fault energy curve for pyramidal II $\langle 11\bar{2}3 \rangle\{11\bar{2}2\}$ slip system in pure magnesium [41]. As plotted in Figure 2, the consequence of in-plane relaxation on the GBSE curve is even more pronounced than in the case of the generalized stacking fault energy curve. While the GBSE is single humped when constraining in-plane relaxation, a local minimum was found when displacing the upper block of atoms by *0.5a* along the $\langle 11\bar{2}0 \rangle$ direction and allowing in-plane relaxation. Although the data plotted in Figure 2 were obtained with the MEAM potential proposed by Kim et al. [14], the other magnesium potentials lead to similar data. All the magnesium potentials predict a single humped GBSE curve when constraining the atomic structure in the in-plane direction, whereas in-plane relaxation leads to a double-humped shape of the GBSE curve independently of the potential. As summarized in Table 2, the energy barrier was found between 135 mJ/m^2 and 257 mJ/m^2 when not allowing in-plane relaxation. When allowing in-plane relaxation, the energy barrier was found between 96 mJ/m^2 and 185 mJ/m^2 while the local minimum was found between 73 mJ/m^2 and 174 mJ/m^2.

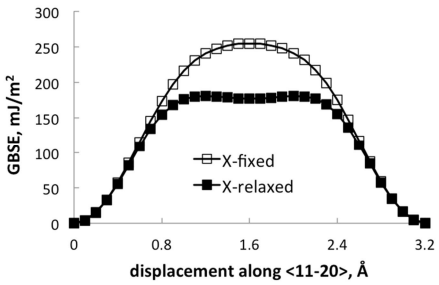

Figure 2. $\{10\bar{1}1\}\langle 11\bar{2}0 \rangle$ GBSE curve in pure magnesium obtained with and without in-plane relaxation. The data plotted in this Figure were calculated with the Kim et al. potential [14].

To reveal the influence of in-plane atomic relaxation (i.e. the shape of the GBSE curve) on the mechanical behavior and strength of the $\{10\bar{1}1\}\langle 11\bar{2}0\rangle$ STGB, quasi-static shear tests were performed on a bicrystal using the different magnesium models. The bicrytals contained 3060 atoms, and their dimensions were about 58Å, 121Å and 10Å along the x, y, and z direction, respectively. The shear tests in static conditions were generated by applying increment of rigid displacement in the z-direction on the cell's top surface followed by minimization of the potential energy using a conjugate gradient relaxation algorithm. The minimum potential energy was assumed to be reached when the maximum force component was below 10^{-6} eV/Å. Although all the models lead to a similar trend, the stress-strain curves obtained with and without in-plane relaxation using the magnesium model of Wu et al. [17] are plotted in Figure 3A for illustration purposes. Following the elastic region, perfect plasticity was observed. The critical shear stresses for activating the mechanism occurring at the STGB are 2.5GPa and 1.8GPa without and with in-plane relaxation, respectively. The decrease of the critical shear stress is in agreement with the one derived from the gradient of the GBSE, which predicts a decrease of the critical shear stress by 15% when considering in-plane relaxation. The corresponding average displacements of the grain boundary along the three directions are plotted in Figure 3B as a function of the shear strain. On one hand, it should be noted that no displacement of the grain boundary along the direction normal to the grain boundary plane was observed when not allowing in-plane relaxation. On the other hand, as illustrated by the snapshots given in Figure 4 and the average displacement along the out-of-plane direction (the direction normal to the STGB plane), grain boundary migration was observed when considering in-plane relaxation.

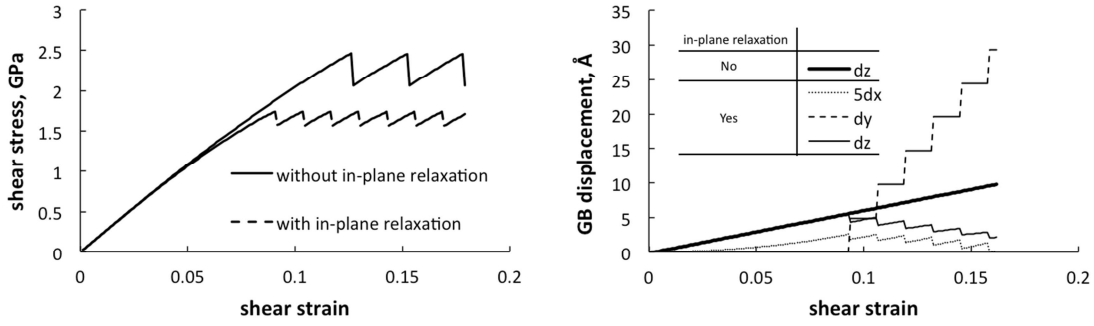

(A) (B)

Figure 3. (A) Strain-stress behavior of the grain boundary structure with and without in-plane relaxation, and (B) displacement of the grain boundary along x, y, and z. Data were obtained with the Wu et al. model [17], and similar observations were made with the other potentials.

Figure 4(A-C) are snapshots extracted from the simulation with in-plane relaxation using the Wu et al. potential obtained at different strain level, 0%, 6% and 12%. At 6% (Figure 4B), the bicrystal behaves elasticity, and the grain boundary remained at its initial location along the out-of-plane direction, while at 12% (Figure 4C), the grain boundary migrated by about 20Å along the out-of-plane direction compared to its original position, leading to a reorientation of the crystal below the grain boundary.

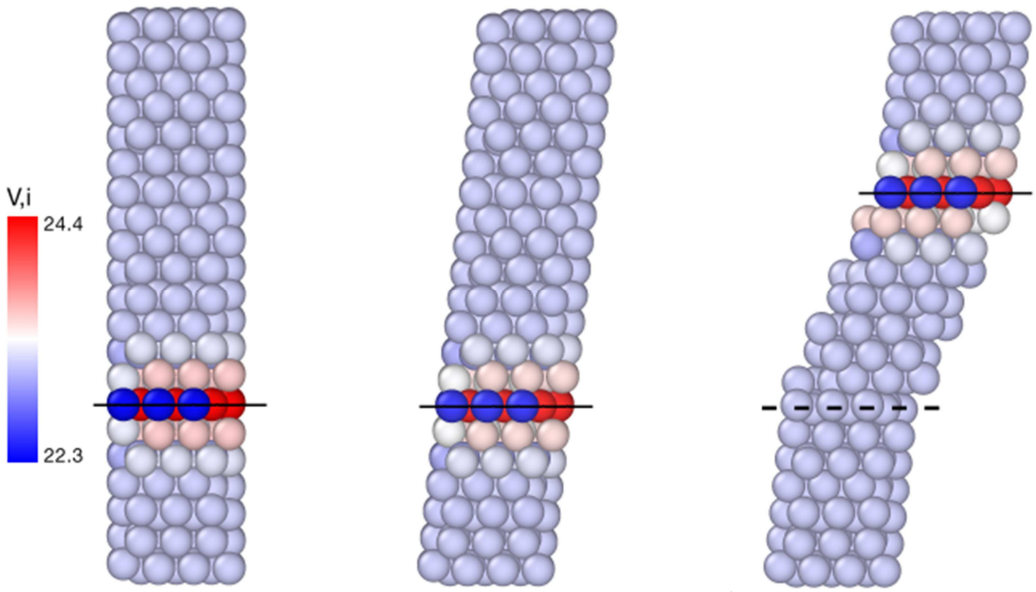

Figure 4. Snapshots extracted from the simulations illustrating grain boundary migration in pure magnesium. (A), (B), and (C) are the grain boundary structures obtained with applied shear stress of 0%, 6%, and 12%. Solid lines indicate the GB plane, while dashed lines indicate the initial location of the GB plane. Atoms are colored based on the atomic volume.

Finally, since the $\{10\bar{1}1\}\langle 11\bar{2}0\rangle$ grain boundary energy ranges between 79 mJ/m^2 and 160 mJ/m^2, the critical shear stress for grain boundary migration was quantified for the different magnesium models. The stress-strain curves modeled with the different potentials are plotted in Figure 5. One can see that the critical stress for grain boundary migration ranges between 0.9GPa and 1.8GPa.

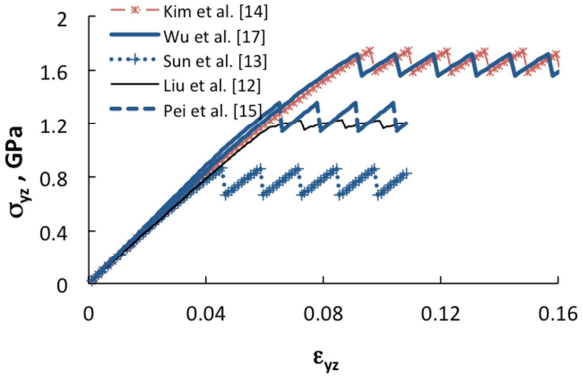

Figure 5. Strain-stress behaviors of the grain boundary structure modeled with the different magnesium interatomic potentials available in the literature.

The data presented in this section, as well the correlation between the grain boundary strength, the grain boundary energy, and the grain boundary sliding energy barrier are discussed in Section 4.1.

3.2 Grain boundary properties in MgX binary alloys

To validate the ability of the MgX binary potentials to model the interaction between a $\{10\bar{1}1\}$ STGB and solute elements of different nature, the segregation energies of solute elements to the atomic sites of maximum contraction and maximum extension were calculated. The predicted segregation energies are summarized in Figure 6, and compared to the first-principles predictions reported by Xi et al. [4]. For comparison purposes, the same setting than Xi et al. [4] was used to predict the segregation energies in the (semi-)empirical potential framework. Qualitatively, apart from the Karewar et al. and Kim et al. potentials for MgLi [25] and MgSn [20], respectively, all the other (semi-)empirical potentials predict segregation sites for Ag, Al, Li, Pb, Ca, Y, and Nd in agreement with first-principles data. Concerning the MgLi and MgSn potentials proposed by Karewar et al. [25] and Kim et al. [20], respectively, the "wrong" trend predicted for the segregation energy in the site of maximum compression and extension compared to the first-principles data are attributed to the inaccuracy of the potentials to predict the volume difference as reported in Table 1. While contraction atomic sites are favored for Ag, Al, Li, Pb, segregation in the extension sites are recovered in the case of Ca, Y and Nd solute elements. The type of atomic sites for segregation of solute elements at the grain boundary is directly related to the atomic volume. Thus, solute elements larger than magnesium segregate in extension sites, while solute elements smaller than magnesium segregate in contraction sites. Quantitatively, although (semi-)empirical potentials predict segregation energies with an error of fifty percent compared to first-principles data, the trend between solute elements obtained by first-principles ($E_{seg}^{Ag} < E_{seg}^{Al} < E_{seg}^{Li} < E_{seg}^{Pb}$) is fully recovered using (semi-)empirical potentials when considering solute elements of smaller dimension than magnesium. When considering solute elements larger than magnesium, it appears from our calculations that (semi-)empirical potentials available in the literature are not accurate enough to reproduce the trend obtained by first-principles calculations. Thus, while first-principles calculations predict the segregation energy of Nd at the grain boundary to be the lowest and of Ca to be the highest, (semi-)empirical potentials predict the segregation energy of Y to be the lowest when considering the Pei et al. potential [15] and the highest when considering the MgY potentials proposed by Lee and coworkers.

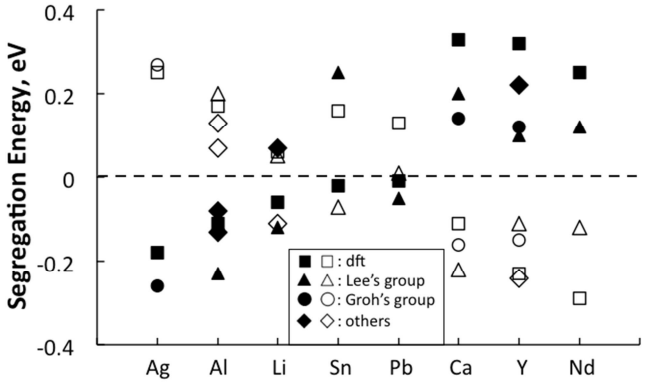

Figure 6: Segregation energies of solute elements in the atomic site of maximum contraction, c1, (filled symbols), and maximum extension, e1, (open symbols). The DFT data were taken from Xi et al. [4].

Since the relaxation of a $\{10\bar{1}1\}$ tilt grain boundary in magnesium involves several extension and contraction atomic sites (see Figure 1), the segregation energy profile along the out-of-plane direction was calculated using the (semi-)empirical potentials that qualitatively predict segregation energy in the site of maximum contraction or extension in agreement with first-principles data. Since all the solute elements smaller than magnesium lead to similar segregation energy profile, Figure 7A illustrates the segregation energy profile along the direction normal to the grain boundary when considering segregation of Al. Similarly, since all the solute elements larger than magnesium lead to a similar segregation energy profile, Figure 7B illustrates the segregation energy profile along the out-of-plane direction when considering segregation of Y. For simplicity reason, since the atomic sites of maximum contraction and extension are located at the same position along the out-of-plane direction (Figure 1B), Figure 7A and B are plotted with the atomic location obtained from a non-relaxed STGB structure. As expected from the analysis of the grain boundary structure, the segregation energies tend to zero when calculated at distance larger than a few angstroms. In the grain boundary region, the segregation energy profiles reveal the location of the extension and contraction sites.

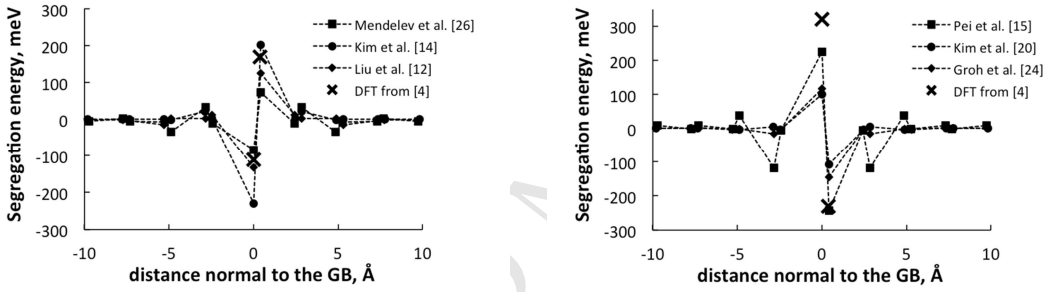

(A) (B)

Figure 7. Segregation energy profile as a function of the distance normal to the $\{10\bar{1}1\}\langle 11\bar{2}0\rangle$ grain boundary when considering Al (A), and Y (B).

The knowledge of the segregation energy profile is of particular importance since it may give access to the concentration of solute elements segregated at the grain boundary by application of segregation theory such as the Langmuir-McLean theory or the White and Coghlan theory. Although some preliminary calculations of the segregation of solute element at the grain boundary performed by a combination of molecular dynamics and Monte Carlo simulations in the grand-canonical ensemble were performed to justify the decoration of the grain boundary by using a regular distribution of segregation, a more detailed analysis of the segregation is currently under investigation, and will be reported elsewhere.

Since no first-principles data revealing the segregation energy profile for the $\{10\bar{1}1\}\langle 11\bar{2}0\rangle$ STGB is available in the literature, the magnitude of the segregation energy at the different sites was compared to the prediction obtained using the elastic model of Huber et al. [5]. Indeed, these authors proposed an elastic model for the solute-GB binding energy. Since the segregation energy is the negative of the binding energy, the same model can be applied in this study. Knowing the atomic volume of site *i* in the grain boundary

structure, the volume of each solute as it exists substitutionally in the magnesium matrix relative to the magnesium atom it has replaced, the magnesium atomic volume, as well as the bulk modulus, the elastic energy between the solute element X and the grain boundary at the atomic site *i* can be written as:

$$E_i^X \approx -B\frac{\Delta V_{bulk}^X}{V_{Mg}}\Delta V_{GB,i} \quad (6)$$

Huber et al. [5] validated the model (Eq. (6)) by correlating the model predictions with the first-principles based segregation energies of nine alloying elements of technological importance (Ag, Ti, Al, Cd, Y, Ca, Nd, Ce, La) segregated at a Σ7 GB.

Figure 8 shows the calculated segregation energy of solute element at site *i* with location R_i, $E_{seg}(\boldsymbol{R_i})$, as a function of the segregation energy predicted by the elastic model proposed by Huber et al. [5].

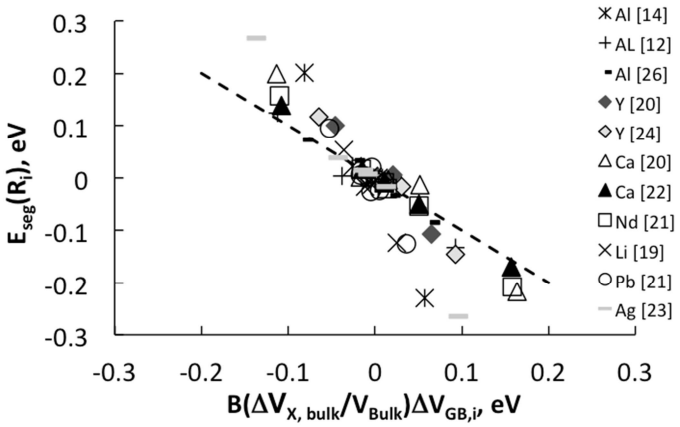

Figure 8. Calculated solute-GB segregation energies plotted against the elastic model of Huber et al. [5]. The dashed lines are a guide for the reader representing Eq. 4 with a proportionality coefficient of 1 between the left and the right hand sides.

As reported in Figure 8, the solute-STGB segregation energies calculated with the (semi-)empirical MgX potentials are in qualitative agreement with the elastic model of Huber et al. [5] when considering a $\{10\bar{1}1\}\langle 11\bar{2}0\rangle$ STGB. Quantitatively, when correlating the entire segregation energies data set calculated in the framework of the (semi-)empirical potentials with a linear functional form, a proportionality factor of 1.5 with the elastic model of Huber et al. [5] was obtained, corresponding to a R^2 value of 0.85. It should be noted, however, that a better correlation was reached when not considering the data set obtained for the MgAg and MgAl binary systems modeled with the potential of Groh and Liu et al. [23, 12], respectively. However, since the potentials were not developed with focus on grain boundary properties, the correlation between the data obtained

with the (semi-)empirical potentials and the one predicted by Eq. (6) is satisfying.

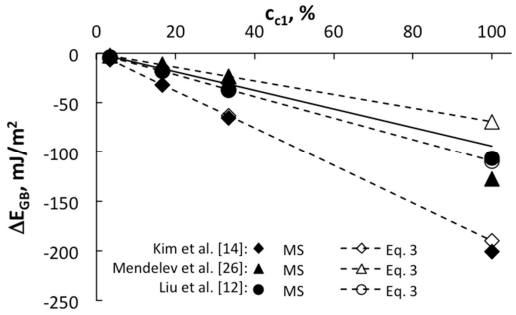

Figure 9. Variation of the grain boundary energies as a function of Al concentration segregated in the contraction sites c1 at the grain boundary. The solid line is a prediction derived from Eq. 3 using the segregation energy at a c1 atomic site obtained from first-principles reported by Xi et al. [4].

Since the preliminary study on the segregation of solute elements at the grain boundary revealed a periodic decoration of the grain boundary in agreement with the data reported by Nie et al. [42], independently of the nature of the solute element, periodic substitution of magnesium atoms by solute elements was carried out at atomic sites with maximum segregation energy to reveal the influence of solute element on (i) the grain boundary energy, (ii) the shape and magnitude of the GBSE curve, and (iii) the stress-strain behavior of the bicrystal.

Variations of the $\{10\bar{1}1\}\langle 11\bar{2}0\rangle$ STGB energy as a function of the concentration of substitutional Al solute elements at the site of maximum contraction, c1, are plotted in Figure 9. It is observed that increasing the concentration of segregated Al at the sites of maximum contraction leads to a decrease of the grain boundary energy. However, while the numerical data obtained by direct molecular statics calculations are in agreement with the theoretical predictions derived from Eq. 3 at low concentration, a divergence between the two predictions is visible at high concentration. In the present study, the concentration is defined as the number of substitutional atoms compared to the total number of atomic sites of maximum contraction/extension. Since the average distance between solute element is decreasing from $3a$ to a (a being the lattice parameter of magnesium) while increasing the solute element concentration from 3.3% to 100%, the interaction between solute elements strongly affect the grain boundary energy changes. Therefore, from the data plotted in Figure 9, one can conclude that predictions derived from Eq. 3 are only valid for concentration of solute element segregated at the grain boundary below 33%, which corresponds to an average distance between solute element of $(3a^2+c^2)^{0.5}$. Compared to the predictions derived from Eq. 3 with the segregation energy obtained from first-principles calculations, one can conclude that a quantitatively good agreement between first-principles predictions and predictions obtained with the Liu et al. [12] and Kim et al. [14] (semi-)empirical potentials was found. On the other hand, the Mendelev et al. MgAl potential [26] overestimates by a factor of 2 the effect of Al solute element on the grain boundary energy changes. A similar effect was

obtained when considering solute elements larger than magnesium, i.e. for solute elements segregating in atomic sites of maximum extension.

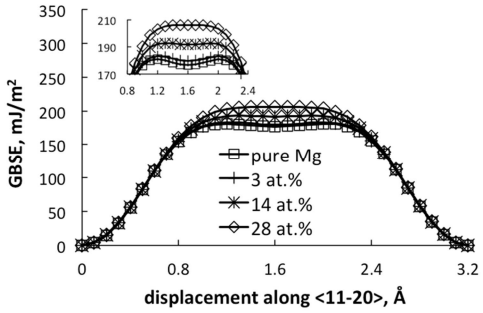

Figure 10. Influence of the Y at.% on the shape and magnitude of the GBSE as a function of the displacement along $\langle 11\bar{2}0\rangle$. Both in-plane and out-of-plane relaxations were considered when predicting the GBSE. The insert focuses on the sliding behavior for displacement around *a/2*. Data were obtained with the Pei et al. potential [15].

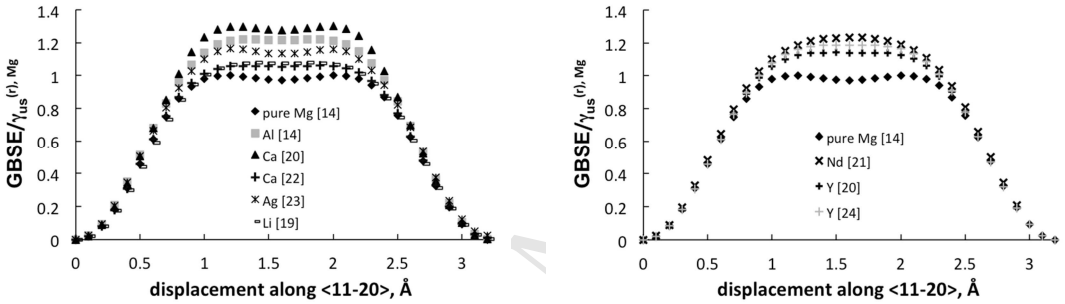

(A) (B)

Figure 11. Influence of 33% of alloying element on the GBSE curves in MgX alloys as a function of the displacement along $\langle 11\bar{2}0\rangle$. Both in-plane and out-of-plane relaxations were considered when predicting the GBSE. The GBSE are normalized by the magnitude of the unstable fault in pure Mg, $\gamma_{us}^{(r)}$. (A) Alloying elements leading to double humped GBSE shape, and (B) Alloying elements leading to single humped GBSE shape

While the influence of in-plane relaxation on the GBSE curves was revealed in pure magnesium (see Fig. 2), calculations were performed using the MgX binary (semi-)empirical potentials to quantify the effect of alloying elements segregated at the $\{10\bar{1}1\}\langle 11\bar{2}0\rangle$ STGB.

Figure 10 represents the GBSE curves obtained with three concentration of Y alloying elements (3 at.%, 14 at.%, and 28 at.%) segregated at the STGB. Overall, while the shape of the GBSE curves depend on the concentration of alloying elements segregated at the grain boundary, the magnitude of the sliding energy barrier increases with increasing the concentration of the alloying elements. Thus, a critical concentration of alloying elements for which a transition from a double-humped shape to a single–humped shape of the GBSE curve can be defined. Figure 11 represents the GBSE curves calculated when considering 33% of atomic sites of maximum contraction/extension on the grain boundary plane occupied by alloying elements with different segregation energies. Since such a

concentration corresponds to an average distance between alloying elements larger than 7.5Å, solute elements are not interacting with each other when calculating the interaction force defined by the gradient of the (semi-)empirical potential. From the analysis of Figure 11A, it appears that segregation of alloying elements with the highest segregation energy leads to a double-humped shape GBSE curves, while a single-humped shape was recovered when considering segregation of alloying elements with the lowest segregation energies (see Figure 11B). Thus, both the segregation energy and the concentration of alloying elements have to be considered if one wants to derive a functional form for the GBSE curve in binary magnesium alloys.

Since the shape of the GBSE curve was found to control the mechanism occurring at the grain boundary in pure magnesium (see Fig. 4), quasi-static shear tests were performed on a bicrystal containing alloying elements segregated at the STGB to validate/disprove whether the shape of the GBSE curve is a dominating factor in activating atomic shuffling occurring at the grain boundary or not. In pure magnesium bicrystal, atomic shuffling is at the origin of grain boundary migration (see Fig. 3). Independently of the nature of the alloying elements, and independently of the mode of relaxation (in-plane and/or out-of-plane) atomic shuffling was not observed in the binary system, and thus grain boundary migration did not occurred. Thus, the shape of the GBSE curve cannot be considered as a dominating factor in activating atomic shuffling in the binary alloys considered in this study. This result is equivalent to the fact that stacking fault energy in binary MgAl alloys is not a dominating factor in determining dislocation velocity [30].

Finally, the critical shear stress differences, $\sigma^{MgX} - \sigma^{Mg}$, for the activation of grain boundary sliding in binary magnesium alloys are plotted in Figure 12 as a function of the segregation energy. Out of all the potentials that predict the location and the magnitude of the segregation energies in agreement with first-principles data (see Fig. 6), two potentials (the MgAl potential proposed by Mendelev et al. [26], and the MgY potential proposed by Kim et al. [20]) predict a softening effect of the grain boundary as a consequence of the presence of segregated alloying elements at the STGB. The trend obtained with these potentials is opposite to the decrease of the grain boundary energy. For the other potentials, the critical shear stress for grain boundary sliding increases with increasing the segregation energy as reported in Figure 12. This finding is in agreement with a decrease of the grain boundary energy with increasing the segregation energy. Furthermore, by making an analogy to the strengthening effect resulting from the interaction between solute element and dislocation, one could make the hypothesis that the strengthening effect resulting from the segregation of alloying element at the $\{10\bar{1}1\}\langle 11\bar{2}0\rangle$ STGB scales with the gradient of the segregation energy at a power n. Further work would be needed to check if such a scaling between the gradient of the segregation energy and the strengthening effect is valid.

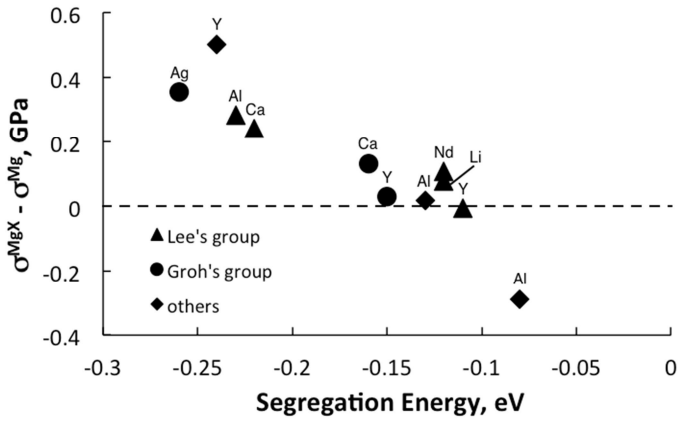

Figure 12. Critical shear stress difference as a function of the segregation energy modeled in MgX binary bicrystal with 33% of the atomic sites of maximum contraction/extension occupied by alloying elements.

4. Discussion

In this study, we presented a systematic investigation using atomistic calculations in the framework of (semi-)empirical potentials to relate intrinsic grain boundary properties to the microscopic and macroscopic behavior of a $\{10\bar{1}1\}\langle 11\bar{2}0\rangle$ STGB in pure magnesium and magnesium binary alloys. Grain boundary energies and the GBSE curve are the main two grain boundary intrinsic properties that were considered in this study, while the critical shear stress for either grain boundary migration or grain boundary sliding were considered as macroscopic quantities. On one hand, while the shape of the GBSE curves controls the microscopic mechanism occurring at the grain boundary in pure magnesium, the data gathered in this study revealed the existence of a direct relationship between the critical shear stress and the grain boundary energy, as well as between the critical shear stress and the energy barrier obtained form the GBSE curves. The observations made in pure magnesium are discussed in section 4.1. On the other hand, while segregation of alloying elements at a $\{10\bar{1}1\}\langle 11\bar{2}0\rangle$ STGB modifies both the shape and the magnitude of the GBSE curves, as well as the grain boundary energies, grain boundary migration was systematically disabled due to the presence of segregated alloying elements. Furthermore, the data suggest the existence of a relationship between the critical shear stress difference and the segregation energy. The observations made in binary magnesium alloys are discussed in section 4.2.

4.1 Pure magnesium

A. Grain boundary sliding energy

As plotted in Figure 2, the shape of the GBSE curve strongly depends whether in-plane relaxation is allowed or not. Since this trend appeared to be potential independent, a small region of the GBSE surface projected in a $\{10\bar{1}1\}$ plane was calculated, and analyzed to demonstrate that only in-plane relaxation can lead to the minimum energy path.

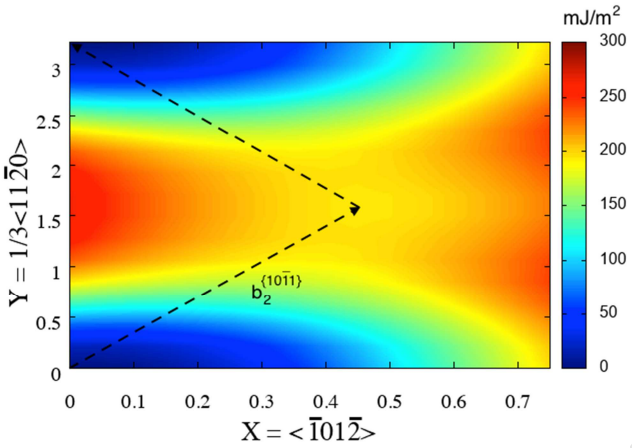

Figure 13. Projection of the GBSE surface in the $\{10\bar{1}1\}$ plane. The path of minimum energy is shown in dashed lines. $b_2^{\{10\bar{1}1\}}$ is the total Burgers vector of the 2-layer twinning dislocation. Data were obtained with the Kim et al. potential [14].

Figure 13 represents the projection in a $\{10\bar{1}1\}$ plane of the GBSE surface obtained by sliding the top grain with respect to the bottom grain along the $\langle\bar{1}01\bar{2}\rangle$ and $\langle11\bar{2}0\rangle$ directions, followed by energy minimization with out-of-plane relaxation and without in-plane relaxation. As represented in Figure 13, $1/3\langle11\bar{2}0\rangle$ is an invariant translation. A local minimum located at about 0.45 Å along the $\langle\bar{1}01\bar{2}\rangle$ direction, and *a/2* along the $\langle11\bar{2}0\rangle$ direction was found. Therefore, the minimum energy path can be defined, as represented in Figure 13 by the dashed lines. One of the two vectors forming the path of minimum energy is the total Burgers vector, $b_2^{\{10\bar{1}1\}}$, of the 2-layer twinning dislocation as discussed by Wang et al. [43]. As a consequence, in-plane relaxation activates the $b_2^{\{10\bar{1}1\}}$ twinning dislocation resulting in grain boundary migration as illustrated in Figure 4 when the shear displacement is applied parallel to the STGB in the $\langle11\bar{2}0\rangle$ direction.

B. Relation between the critical shear stress and the (i) GB energy, and (ii) the energy barrier

Figure 14A represents the critical shear stress as a function of the grain boundary energy normalized by the surface energy modeled with both the different magnesium potentials. As expected, it is observed that an increase of the grain boundary energy leads to a decrease of the critical shear stress. When dissociating the data gained with the EAM potentials from the ones gathered with the MEAM potentials, a linear correlation between the critical shear stress and the grain boundary energy can be established with a correlation factor, R^2, close to 0.99 and 0.96 for the MEAM and EAM data. In addition, as represented in Figure 14B, the data obtained in this study suggest the energy barrier derived from the GBSE curve to be proportional to the grain boundary energy. Although the correlation factor between the energy barrier and the grain boundary energy is close to 0.97 when considering the data obtained with potentials parameterized in the MEAM framework, such correlation factor decrease to 0.42

when considering data gathered with potentials derived in the EAM framework. Such a difference between the MEAM and the EAM data is attributed to the long-range interaction, and to significant difference in the parameterization of the EAM potentials. However, since the mechanism occurring at the grain boundary during shear testing was not affected by the nature of the magnesium potentials, our data suggest that (i) the grain boundary energy controls the magnitude of the critical shear stress, and (ii) the shape of the GBSE controls the mechanism occurring at the grain boundary.

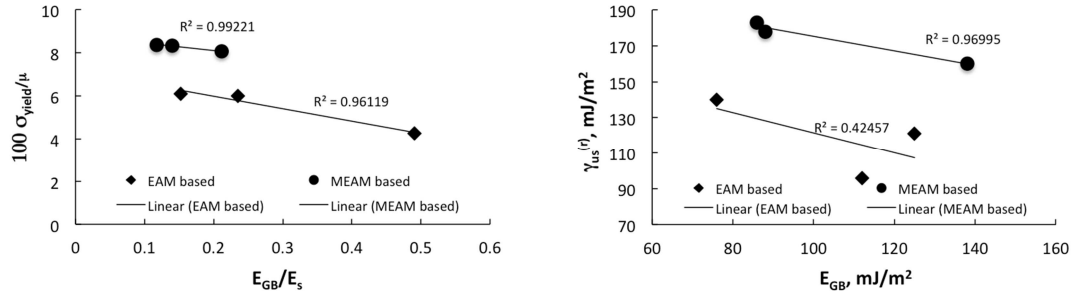

(A) (B)

Figure 14. Variation of (A) the critical shear stress normalized by the shear modulus as a function of normalized grain boundary energy, and (B) the grain boundary energy barrier along $\langle 11\bar{2}0\rangle$, $\gamma_{us}^{(r)}$, as a function of the GB energy.

4.2 Binary magnesium alloys

As reported in Figure 10, segregation of solute elements at the grain boundary modifies both the shape of the GBSE curves, and the magnitude of the grain boundary sliding energy barrier. These changes depend on (i) the concentration of segregated elements, and (ii) the chemical nature of the alloying elements defined by its segregation energy.
Independently of the (semi-)empirical potentials, the grain boundary sliding energy barrier increases with increasing the concentration of alloying elements segregated at the grain boundary. However, since the GBSE curves are predictions obtained with the (semi-)empirical models, the transition from a double-humped shape to a single-humped shape of the GBSE as a function of the concentration of alloying elements has to be confirmed using first-principles calculations. Furthermore, such behavior derived from first-principles calculations is envisioned to be part of the materials database for developing or testing new empirical potentials for binary alloys.

At low concentration of alloying elements segregated at the grain boundary, the grain boundary sliding energy was analyzed as a function of the grain boundary changes. The data plotted in Figure 15A and B revealed a clear relationship between these two quantities, the grain boundary sliding energy barrier increases with decreasing the grain boundary energy due to the presence of alloying elements. Thus, from a macroscopic perspective, the strengthening of a $\{10\bar{1}1\}\langle 11\bar{2}0\rangle$ STGB due to the presence of alloying elements can be modeled as a function of the grain boundary energy, the grain boundary sliding energy, or the segregation energy.

However, since the deformation mechanism occurring at the grain boundary is independent of the shape of the GBSE, the grain boundary sliding energy barrier is not thought to be the most critical material parameter for modeling grain boundary sliding in magnesium-based binary alloys.

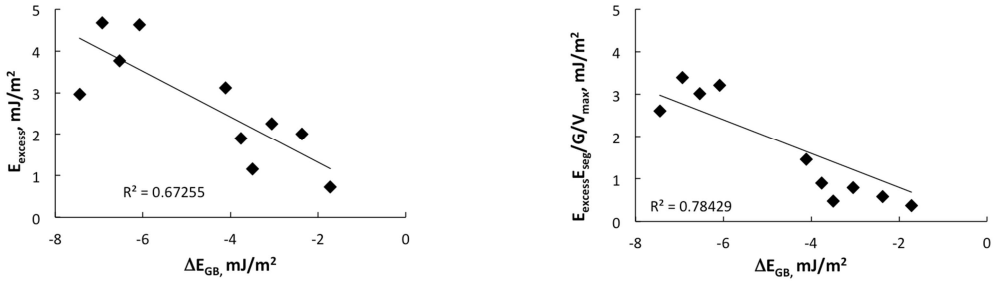

(A) (B)

Figure 15. Excess energy vs grain boundary energy at a constant concentration of alloying elements. (A) not normalized (B) normalized

5. Concluding remarks

In this study, we investigated the relationships between the grain boundary strength, the grain boundary energy, the grain boundary sliding energy barrier, the shape of the GBSE, and the segregation energies using (semi-)empirical potentials at 0K. The conclusions of this study are summarized as follow:

1. MgX (semi-)empirical potentials were benchmarked with respect to segregation energies for solute elements segregated at a $\{10\bar{1}1\}\langle 11\bar{2}0\rangle$ STGB. It was found that out of all the MgX binary potentials, the MgSn potential proposed by Kim et al. [20], the MgLi potential developed by Karewar et al. [25], and the MgAl potential published by Jelinek et al. [16] are not accurate enough to predict segregation of the alloying elements at the atomic site of maximum compression. All the other potentials predict segregation energies at the site of maximum extension/contraction in agreement with first-principles data. Out of all the (semi-)empirical potentials predicting the site of maximum segregation energy in agreement with first-principles data, the MgAl potential proposed by Mendelev et al. [26] and the MgY potential proposed by Kim et al. [20] lead a softening of the critical shear stress in the presence of alloying element segregated at the STGB grain boundary.

2. The effects of out-of-plane and in-plane atomic relaxation on the shape and magnitude of the GBSE curve were studied. It was found that out-of-plane relaxation controls the magnitude of the sliding energy barrier without altering the overall shape of the GBSE curve, while in-plane relaxation controls the shape of the GBSE curve. The GBSE curve transforms from a single humped shape to a double humped shape when considering in-plane relaxation. These findings are similar to what was already reported when considering in-plane and out-of-plane relaxation effects on the generalized stacking fault energy curves.

3. The effect of the GBSE shape, i.e. of the relaxation procedure, was revealed during simple shear of bicrystal at 0K. With in-plane relaxation, grain boundary migration by nucleation of the 2-layer twinning dislocations with Burgers vector $b_2^{\{10\bar{1}1\}}$ was modeled when the shear displacement was applied parallel to the STGB in the $\langle 11\bar{2}0\rangle$ direction.

4. A relationship between the critical shear stress and the grain boundary energy was obtained. The critical shear stress decreases with increasing the grain boundary energy. While the MEAM data suggests a relationship between the grain boundary energy and the grain boundary sliding energy barrier, the lack of relation revealed by the EAM data do not allow the authors to conclude that the grain boundary sliding energy barrier is a material property controlling the critical shear stress at 0K. Further investigation would be required to validate/disprove whether the grain boundary sliding energy barrier is a critical material parameter under creep condition or not.

5. The effect of alloying elements on both the grain boundary energy, and the shape and magnitude of the GBSE curves were studied. These intrinsic materials properties were correlated with the critical shear stress. As expected, our data allowed us to recover the interplay between the grain boundary energy and the critical shear stress, i.e. an increase in grain boundary energy leads to a decrease of the critical shear stress. Furthermore, by increasing the concentration of segregated element at the grain boundary, the GBSE curve transforms from a double humped to a single humped shape. The critical concentration for the transition between single-humped to double-humped is material dependent.

6. In the alloy systems, the $\{10\bar{1}1\}\langle 11\bar{2}0\rangle$ STGB was pinned by the alloying elements. As a consequence, since segregation of alloying elements at the $\{10\bar{1}1\}\langle 11\bar{2}0\rangle$ STGB disabled grain boundary migration, the shape of the GBSE curve cannot be considered as a critical material behavior in the alloy system for the $\{10\bar{1}1\}\langle 11\bar{2}0\rangle$ STGB, and thus for grain boundary in general.

Acknowledgments

The authors acknowledge the MIRACLE Project at the University of Basel funded by the Werner Siemens Foundation, Zug/Switzerland, to support this study. Calculations were performed at sciCORE (http://scicore.unibas.ch/) scientific computing core facility at the University of Basel. The authors thank the anonymous referees for their insights that resulted in crucial improvement of the manuscript.

Reference:

[1] H. Somekawa, T. Mukai, 2012. Effect of grain boundary structures on grain boundary sliding in magnesium. *Materials Letters* **76** 32-35.

[2] H. Somekawa, H. Watanabe, T. Mukai, 2014. Effect of solute atoms on grain boundary sliding in magnesium alloys. *Phil. Mag.* **94** 1345-1360.

[3] J. Zhang, Y. Dou, Y. Zheng, 2014. Twin-boundary segregation energies and solute-diffusion activation enthalpies in Mg-based binary system: a first-principles study. *Sc. Mater.* **80** 17-20.
[4] G. Xi, J. Zhang, C. Fang, 2016. Effects of alloying elements on the cohesion of {10-11} twin boundary from first-principles calculations. *Mater. Letters* **182** 198-200.
[5] L. Huber, J. Rottler, M. Militzer, 2014. Atomistic simulation of the interaction of alloying elements with grain boundaries in Mg. *Acta Mater.* **80** 194-204.
[6] M.A. Bhatia, S.N. Mathaudhu, K.N. Solanki, 2015. Atomic-scale investigation of creep behavior in nanocrystalline Mg and Mg-Y alloys. *Acta Mater.* **99** 382-391.
[7] C.D. Barrett, H. El Kadiri, R. Moser, 2017. Generalized interfacial fault energies. *International Journal of Solids and Structures* **110-111** 106-112.
[8] R. Reddy, S. Groh, 2016. Atomistic modeling of the effect of calcium on the yield surface of nanopolycrystalline magnesium-based alloys. *Comp. Mater. Sci.* **112** 219-229.
[9] S. Karewar, N. Gupta, S. Groh, E. Martinez, A. Caro, S.G. Srinivasan, 2017. Effect of Li on the deformation mechanisms of nanopolycrystalline hexagonal close packed magnesium. *Comp. Mater. Sci.* **126** 252-264.
[10] S. Groh, M. Alam, 2015. Fracture behavior a lithium single crystal in the framework of (semi-)empirical force field derived from first-principles. *Modelling Simul. Mater. Sci. Eng.* **23** 045008.
[11] G. Zu, S. Groh, 2016. Effect of segregated alloying element on the intrinsic fracture behavior of Mg. *Theo. Appl. Frac. Mech.* **85** 236-245.
[12] X.Y. Liu, J.B. Adams, F. Ercolessi, J.A. Moriarty, 1996. EAM potential for magnesium from quantum mechanical forces. *Modelling Simul. Mater. Sci. Eng.* **4** 293.
[13] D.Y. Sun, M.I. Mendelev, C.A. Becker, K. Kudin, T. Haxhimali, J.J. Hoyt, A. Karma, D.J. Srolovitz, 2006. Crystal-melt interfacial free energies in hcp metals: A molecular dynamics study of Mg. *Phys. Rev. B* **73** 024116.
[14] Y.-M. Kim, N.J. Kim, B.-J. Lee, 2009. Atomistic modeling of pure Mg and Mg-Al systems. *CALPHAD: Comp. Coupl. Phase Diag. Themo*. **33** 650-657.
[15] Z. Pei, L.-F. Zhu, M. Friák, S. Sandlöbes, J. von Pezold, H.W. Sheng, C.P. Race, S. Zaefferer, B. Svendsen, D. Raabe, J. Neugebauer, 2013. Ab initio and atomistic study of generalized stacking fault energies in Mg and Mg-Y alloys. *New Journal of Physics* **15** 043020.
[16] B. Jelinek, S. Groh, M.F. Horstemeyer, J. Houze, S.G. Kim, G.J. Wagner, A. Moitra, M.I. Baskes, 2012. Modified embedded atom potential for Al, Si, Mg, Cu, and Fe alloys. *Phys. Rev. B* **85** 245102.
[17] Z. Wu, M.F. Francis, W.A. Curtin, 2015. Magnesium interatomic potential for simulating plasticity and fracture phenomena. *Modelling Simul. Mater. Sci. Eng.* **23** 015004.
[18] S. Groh, M.K. Nahhas, Modeling dislocation in binary magnesium alloys using atomistic method, Mechanics of Materials. Nanomechanics, serie, ed. C.H. Hsuesh, C.-S. Chen, S. Schmauder, W. Chen. In press.
[19] Y.-M. Kim, I.-H. Jung, B.-J. Lee, 2012. Atomistic modeling of pure Li and Mg-Li system. *Modelling Simul. Mater. Sci. Eng.* **20** 035005.
[20] K.-H. Kim, J. B. Jong, B-.J. Lee, 2015. Modified embedded-atom method interatomic potentials for Mg-X (X = Y, Sn, Ca) binary systems. *CALPHAD: Comp. Coupl. Phase Diag. Themo*. **48** 27-34.

[21] K.-H. Kim, B.-J. Lee, 2017. Modified embedded-atom method interatomic potentials for Mg-Nd and Mg-Pb binary systems. *CALPHAD: Comp. Coupl. Phase Diag. Themo*. **57** 55-61.
[22] S. Groh, 2015. Mechanical, thermal, and physical properties of Mg-Ca compounds in the framework of the modified embedded-atom method. *J. Mech. Behav. Biomed. Mater.* **42** 88-99.
[23] S. Groh, 2016. Modified embedded-atom potential for B2-MgAg. *Modelling Simul. Mater. Sci. Eng.* **24** 065011.
[24] S. Groh, Modified embedded-atom potential for MgY. *In preparation*.
[25] S. Karewar, N. Gupta, A. Caro, S. Srinivasan. 2014. A concentration dependent embedded atom method potential for the MgLi system. *Comp. Mater. Sci.* **85** 172-178.
[26] M.I. Mendelev, M. Asta, M.J. Rahman, J.J. Hoyt, 2009. Development of interatomic potentials appropriate for simulation of solid-liquid interface properties in Al-Mg alloys. *Phil. Mag.* **89** 3269-3285.
[27] L. Shen, G. Proust, G. Ranzi, 2010. An atomistic study of dislocation-solute interaction in Mg-Al alloys. *IOP Conf. Series: Mater. Sci. Eng.* **10** 012177.
[28] L. Shen, 2013. Molecular dynamics study of Al solute-dislocation interactions in Mg Alloys. *Interaction Multiscale Mechanics* **6** 127-136.
[29] W. Xiao, X. Zhang, W.T. Geng, G. Lu, 2013. Atomistic study of plastic deformation in Mg-Al alloys. *Mater. Sci. Eng. A 586* 245-252.
[30] P. Yi, R.C. Cammarata, M.L. Falk, 2016. Atomistic simulation of solid solution hardening in Mg/Al alloys: Examination of composition scaling and thermo-mechanical relationships. *Acta Mater.* **105** 378-389.
[31] K.H. Kim, J.B. Jeon, N.J. Kim, B.-J. Lee, 2015. Role of yttrium in activation of <c+a> slip in magnesium: An atomistic approach. *Scr. Mater.* **108** 104-108.
[32] H. Somekawa, T. Mukai, 2013. Molecular dynamics simulation of grain boundary plasticity in magnesium and solid-solution magnesium alloys. *Comput. Mater. Sci.* **77** 424-429.
[33] M. Ghazisaeidi, L.G. Hector Jr, W.A. Curtin, 2014. Solute strengthening of twinning dislocations in Mg alloys. *Acta Mater.* **80** 278-287.
[34] N. Miyazawa, T. Yoshida, M. Yuasa, Y. Chino, M. Mabushi, 2015. Effect of segregated Al on {10-12} and {10-11} twinning in Mg. *J. Mater. Res.* **30** 3629-3641.
[35] S. Plimpton, 1995. Fast parallel algorithms for short-range molecular dynamics. *J. Comput. Phys.* **117** 1-19.
[36] A. Stukowski, 2010. Visualization and analysis of atomistic simulation data with ovito-the open visualization tool. *Modell. Simul. Mater. Sci. Eng.* **18** 015012.
[37] J. Wang, I.J. Beyerlein, 2012. Atomic structures of symmetric tilt grain boundaries in hexagonal close packed (hcp) crystal. *Modelling Simul. Mater. Sci. Eng.* **20** 024002.
[38] P. Kwaśniak, P. Śpiewak, H. Garbacz, K.J. Kurzydłowski, 2014. Plasticity of hexagonal systems: Split slip modes and inverse Peierls relation in α-Ti. *Phys. Rev. B* **89** 144105.
[39] Y. Dou, J. Zhang, 2015. Effect of structural relaxation on the generalized stacking fault energies of hexagonal-close-packed system from first-principles calculation. *Comp. Mater. Sci.* **98** 405-409.

[40] J.A. Zimmerman, H. Gao, F.F. Abraham. 2000. Generalized stacking fault energies for embedded atom FCC metals. *Modelling Simul. Mater. Sci. Eng.* **8** 103-115.

[41] A. Kumar, B.M. Morrow, R.J. McCabe, I.J. Beyerlein, 2017. An atomic-scale modeling and experimental study of <c+a> dislocations in Mg. *Mater. Sc. Eng. A* **695** 270-278.

[42] J.F. Nie, Y.M. Zhu, Z. Liu, X.Y. Fang, 2013. Periodic segregation of solute atoms in fully coherent twin boundaries. *Science* **340** 957-960.

[43] J. Wang, I.J. Beyerlein, J.P. Hirth, C.N. Tomé, 2011. Twinning dislocations on $\{\bar{1}011\}$ and $\{\bar{1}013\}$ planes in hexagonal close-packed crystals. *Acta Mater.* **59** 3990-4001.

We performed atomistic calculation to reveal the effect of segregated solute elements on the mechanical properties of a symmetrical tilt grain boundary

Increasing the concentration of segregated solute element transforms the grain boundary sliding energy (GBSE) curve from single humped to double humped.

The shape of the grain boundary sliding energy curve cannot be considered as a critical material property to describe a grain boundary in magnesium-binary alloys